



Dissolution behavior of dizinc magnesium phase in Al–Zn–Mg–Cu alloy

Hongfu Yang¹ · Yelin Zhang¹ · Shanju Zheng¹ · Zaki I. Zaki² · Rensong Huang¹ · Shumeng Lu¹ · Peng Sun¹ · Mohamed M. Ibrahim² · Hua Hou³ · Mengnie Li¹ · Xiaohong Yuan⁴ · Xiaojing Wang⁵ · Zein M. El-Bahy⁶

Received: 24 August 2023 / Revised: 30 October 2023 / Accepted: 2 November 2023 / Published online: 23 November 2023
© The Author(s), under exclusive licence to Springer Nature Switzerland AG 2023

Abstract

The presence of the dizinc magnesium ($MgZn_2$) phase in Al–Zn–Mg–Cu alloy significantly enhances its mechanical properties due to the high density, uniform distribution, and fine size of the $MgZn_2$ phase. While previous studies have focused on precipitation evolution during solid solution and aging, little attention has been given to dissolution behavior. The dissolution behavior of $MgZn_2$ phase during heat treatment was studied by changing the heat treatment temperature and time in the article. It was found to be completely dissolved at 480 °C and 490 °C/60 min. Experimental results were fitted to establish the relationship between the volume fraction of the $MgZn_2$ phase and time at temperatures ranging from 460 to 490 °C. Additionally, a kinetic model for dissolution process was derived based on classical particle system dissolution model and diffusion-controlled transformation theory with adjusted parameters representing physical quantities accurately. These results are helpful to obtain precipitates with smaller size, more quantity and better dispersion, which is of great significance for improving the mechanical properties of the alloy.

Keywords Dizinc magnesium phase · Dissolution behavior · Kinetic model · Al–Zn–Mg–Cu alloy

Hongfu Yang and Yelin Zhang contributed equally to this work.

✉ Shanju Zheng
zhengshanju1@163.com

✉ Xiaohong Yuan
yxhong87@163.com

✉ Xiaojing Wang
wxj@just.edu.cn

¹ Faculty of Material Science and Engineering, Kunming University of Science and Technology, Kunming 650093, China

² Department of Chemistry, College of Science, Taif University, P.O. Box 11099, Taif 21944, Saudi Arabia

³ School of Materials Science and Engineering, Taiyuan University of Science and Technology, Taiyuan 030024, China

⁴ Sino-Platinum Metals Co. Ltd., Kunming Institute of Precious Metals, Kunming 650106, China

⁵ Jiangsu University of Science and Technology, Zhenjiang 212003, China

⁶ Department of Chemistry, Faculty of Science, Al-Azhar University, Nasr City, 11884 Cairo, Egypt

1 Introduction

Al–Zn–Mg–Cu alloy is a heat treatable aluminum alloy that has gained wide application in the aerospace, automotive, and rail transit industries [1–3]. With advancements in aviation, transportation, and other fields, there is a growing demand for ultra-high-strength aluminum alloy materials with enhanced strength, toughness, and corrosion resistance. Researchers have made efforts to improve the overall properties of this alloy through optimization of its composition, enhancements in the heat treatment process, and the development of new molding methods [4–8]. Among the treatment methods, solid solution and aging heat treatment have received considerable attention for effectively improving the properties of Al–Zn–Mg–Cu alloys. During this treatment, after the alloy undergoes solution heat treatment and water quenching, a substantial number of Zn, Mg, and Cu atoms dissolve into the matrix, forming a supersaturated solid solution. The solute atoms and vacancies create a chemical driving force that strengthens precipitation during aging [9, 10]. The supersaturated solid solution begins to decompose, forming solute atoms known as GP I and GP II. GP (I) regions are generated through the substitution and ordering of solute atoms along the Al lattice, while GP (II) regions are zinc-rich layers found on the {111} Al

plane. Notably, when the alloy is quenched from a solution temperature above 450 °C, this decomposition occurs along the $\langle 110 \rangle$ Al direction [11]. The precipitation behavior of the Al–Zn–Mg–Cu alloy can be summarized as follows: supersaturated solid solution (SSSS) → GP zones (GP I and II) → η' precipitates → η precipitates [12]. In Al–Zn–Mg–Cu aluminum alloy, η phase has a space group of P_{63}/mmc , and its equilibrium stoichiometric composition is usually close to $MgZn_2$, which is called the hexagonal C_{14} Laves phase [13]. The precipitated phase significantly influences the properties of the alloy. Pikee Priya et al. [14] focused on investigating the precipitation process during post-homogenization cooling. The researchers developed a numerical model based on the particle size distribution (PSD) to predict the diffusion-based nucleation, growth, and coarsening of plate-like precipitates. Yang et al. [15] characterized the morphology of the η phase as the primary strengthening precipitate using transmission electron microscopy. They also analyzed the orientation and electron diffraction pattern of the η precipitate through transition matrix calculations, revealing that there were only three different zone axes in the four variants, all parallel to the $[110]$ Al direction of the Al matrix.

However, current research on the η phase of the Al–Zn–Mg–Cu alloy primarily focuses on its precipitation behavior, microstructure, orientation relationship, and impact on alloy properties after solution aging. The dissolution behavior of η phase in the heat treatment process has not been studied. The dissolution of the second phase in an aluminum alloy is mainly influenced by temperature and time. Dissolution is the most important phase transformation process in the solid solution treatment process of the material. The degree of dissolution directly affects the super-saturation level of strengthening elements, precipitation driving force during aging stage, number of precipitates formed, as well as strength and toughness characteristics of aged aluminum alloys related to aging precipitation behavior. The essence of dissolution is atomic diffusion. In recent years, numerous scholars [16, 17] have used the quantification and modeling of the atomic thermal motion rate in the phase transition process of aluminum alloy to study the atomic motion mechanism. Based on Fick's law of diffusion [18, 19], Whelan [20] proposed a widely used volume diffusion kinetic model for second phase dissolution. Increasing the degree of second phase dissolution within the matrix effectively enhances driving forces for subsequent phase transformation processes such as aging precipitation by reducing critical nucleation radii for precipitated phases

resulting in smaller size, higher number density, better dispersion characteristics, and improved strengthening effects. Therefore, quantifying and modeling second phase dissolution behaviors during solid solution stages holds significant engineering application value for optimizing performance while minimizing costs.

This study aims to investigate the effect of varying solution heat treatment temperature and time on the dissolution behavior of the η phase using scanning electron microscopy (SEM) and transmission electron microscopy (TEM, HRTEM). The kinetic equation for the η phase dissolution process is constructed. The relationship between the dissolution process of the η phase and mechanical properties is analyzed through Vickers hardness testing. In this paper, the morphology and distribution of η phase in Al–Zn–Mg–Cu alloy during heat treatment and its dissolution behavior in solid solution process were studied for the first time, and the dissolution model was established. By solving the kinetic model, the variation of the dissolution volume fraction of the second phase with time during the solid solution process is obtained, and the time required for the complete dissolution of the second phase is calculated by the model, which provides theoretical guidance for engineering applications. Additionally, considering that the η phase can dissolve and precipitate during hot processing, the findings serve as a reference for understanding the evolution of the η phase during hot deformation. Furthermore, considering that hot deformation can lead to both precipitation and dissolution of η phases, our results serve as a reference for understanding their evolution during such processes.

2 Experimental materials and methods

2.1 Preparation of cast Al–Zn–Mg–Cu alloy

The composition of the Al–Zn–Mg–Cu alloy is presented in Table 1. The experimental alloy had a melting temperature of 720 °C, and the pouring temperature ranged from 690 to 710 °C. For all alloys, high-purity raw materials were utilized, including Al (99.99 pct), Al-50 (Cu, Mg, and Cr), Al-30Zn, Al-10Zr, and Al-10Ti, by the nominal compositions (mass fraction) of 7050 alloy. These raw materials, standard component alloys, were purchased specifically for smelting. To obtain the Al–Zn–Mg–Cu ingots, a medium-frequency induction furnace was employed to facilitate the melting process of the raw materials. Subsequently, the resulting molten alloys were cast into a cast iron mold.

Table 1 Chemical composition of Al–Zn–Mg–Cu Alloy (Wt. %)

Elements	Zn	Mg	Cu	Fe	Si	Cr	Mn	Ti	Zr	Al
Contents	6.431	2.210	2.152	0.258	0.105	0.305	0.097	0.058	0.177	Bal

2.2 Experimental procedures

The alloys underwent a two-step homogenization process at 466 °C for 36 h, followed by 470 °C for 24 h, and were subsequently cooled with the furnace. Subsequently, a second phase solution heat treatment was conducted at temperatures of 460 °C, 470 °C, 480 °C, and 490 °C for durations of 5 min, 10 min, 30 min, and 60 min, respectively (refer to Fig. S1). The SEM samples were polished with alumina solution after sandpaper polishing. The elemental distribution in the alloys was decided by applying a JXA-8230 electron probe micro-analyzer (EPMA). The microstructure of the samples was examined using TEM (FEI Chennai G2 F20) and SEM (a JSM-7800F) with EDS. The SEM operated at a voltage of 15 kV, and to obtain a clearer second phase, backscattered electrons were used to boost the contrast. The microstructures of the second phase were analyzed using an FEI Chennai G2 F20 TEM equipped with an energy-dispersive X-ray spectrometer (EDS). The interface microstructures of MgZn₂/Al were investigated using high-resolution TEM (HRTEM). TEM discs were punched out from foils with a thickness of approximately 60 μm and electro-polished in a twin-jet polishing machine using a solution comprising two-thirds methanol (CH₃OH) and one-third nitric acid (HNO₃) at a temperature ranging between –20 and –30 °C. The area of the MgZn₂ phase was measured in a minimum of eight back-scattered electron images utilizing picture analysis software (Image-J). The 3S-1000QDZ optical hardness tester was used to test each alloy sample 10 times, and the average hardness value of each alloy was calculated.

3 Result and discussion

3.1 Thermodynamic equilibrium phase

Figure 1a shows the equilibrium phase composition of the Al-Zn-Mg-Cu alloy, calculated using JMatPro software, excluding the liquid phase and Al matrix from the diagram. The solid phase transformation of the alloy initiates at 514 °C, below the solidus temperature. Sequential precipitation of the E-(AlCrMgMn) phase, Mg₂Si phase, Al₇Cu₂Fe phase, S (Al₂CuMg) phase, Al₆Mn phase, and η(MgZn₂) phase occurs from the α (Al) solid solution. The equilibrium phase composition of the Al-Zn-Mg-Cu alloy at room temperature consists of 65.67% α (Al), 9.12% η, 2.53% S, 2.06% E, 0.51% Al₆Mn, 0.34% Al₇Cu₂Fe, and 0.18% Mg₂Si, with the η phase serving as the primary strengthening phase. Heat treatment from 460 to 490 °C was chosen to investigate the dissolution behavior of the η (MgZn₂) phase. To predict the effect of aging precipitation strengthening on the properties and microstructure of Al-Zn-Mg-Cu alloy after solution treatment, the composition of the alloy's metastable

phase was calculated using JMatPro software, as depicted in Fig. 1b. The results reveal that the metastable phases in the alloy include the S' phase, Q' phase, β' phase, Al₃Zr-L1₂ phase, and η' phase, with the η' phase being the primary metastable phase. The desolvation sequence during aging in the Al-Zn-Mg-Cu alloy generally follows SSSS → GP zones (GPI and II) → η' precipitates → η precipitates [21]. Notably, the η' phase exhibits a semi-coherent relationship with the matrix, serving as the primary precipitated strengthening phase of the alloy, which is consistent with the simulation results of the metastable phase.

Figure 1c illustrates the TTT curve of the Al-Zn-Mg-Cu alloy, depicting an overall “C” shape. The GP zone has the lowest starting transition temperature at 160 °C, with the nose temperature and corresponding incubation time recorded as 140 °C and 5.73 s, respectively. Subsequently, the nose temperatures of the remaining phases, η', S', η (MgZn₂), and S phase, increase sequentially to 340 °C, 300 °C, 390 °C, and 410 °C, with corresponding incubation times of 23.64 s, 22.48 s, 26.73 s, and 17.63 s, respectively. Figure 1d shows the CCT curve of the Al-Zn-Mg-Cu alloy, which comprehensively illustrates the relationship between phase transformation, temperature, and time during the continuous cooling transformation of the alloy, providing the heat treatment process design an important reference for aluminum alloys. Based on the calculation results, the critical cooling rates for the GP zone, η (MgZn₂), and S phase are 0.69 °C/s, 166.6 °C/s, and 55.5 °C/s, respectively. Considering the TTT curve, it can be observed that the cooling rate of the Al-Zn-Mg-Cu alloy exceeds 166.6 °C/s. Furthermore, when the cooling time of the sample solution is less than 5.73 s, it effectively suppresses the precipitation of other phases, resulting in the formation of a supersaturated solid solution.

3.2 MgZn₂ phase distribution and structure

Figure 2 shows the element distribution of the Al-Zn-Mg-Cu alloy following homogenization treatment and slow cooling with a furnace. The alloy's second phase demonstrates uniform precipitation after homogenization, with a predominantly rod-like and needle-like morphology and relatively uniform distribution. Based on the elemental composition and morphological characteristics, the dispersed phase is identified as the MgZn₂ phase, which aligns with previous reports [14, 22]. From a distribution standpoint, the MgZn₂ phase exhibits a high-density dispersion pattern after homogenization. This marks the instance of the MgZn₂ phase dissolving into the aluminum matrix during homogenization, with uniform atomic diffusion driven by thermal factors [23]. Some of the second phases display evident coarsening as nucleation sites at defects grow and enlarge. Research has shown that the coarsened

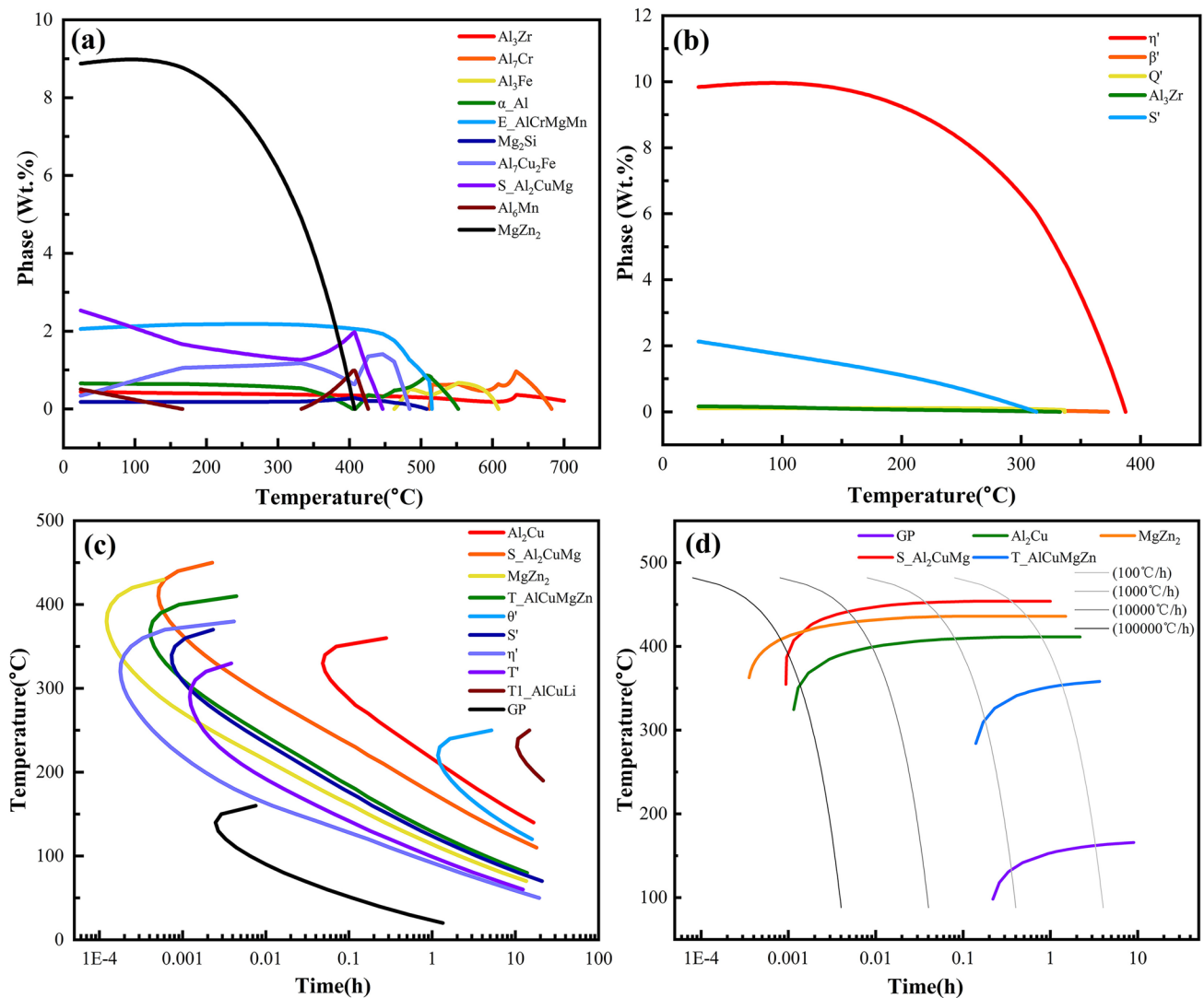


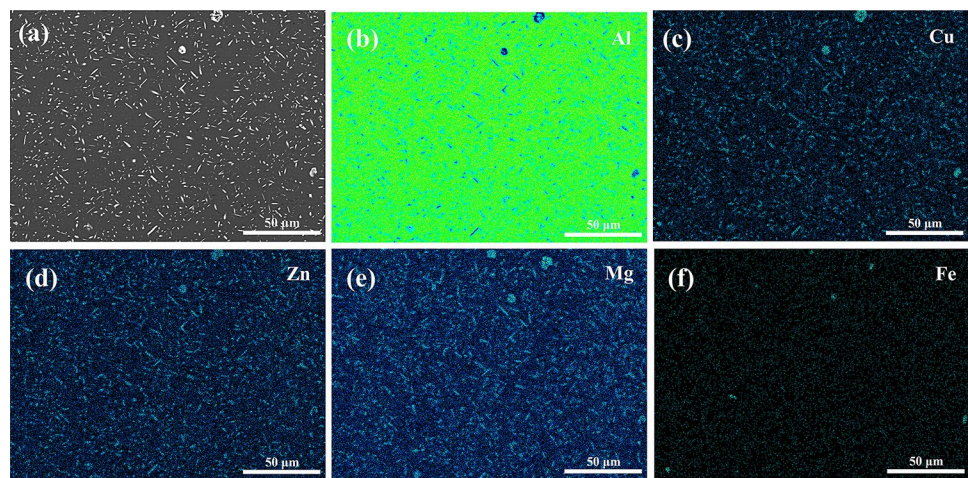
Fig. 1 a Al–Zn–Mg–Cu alloy equilibrium phase diagram; b Al–Zn–Mg–Cu alloy metastable phase; c Al–Zn–Mg–Cu alloy TTT curve; d Al–Zn–Mg–Cu alloy CCT curve

second phase is located at dislocations [24]. It is observed that certain coarser phases are enriched with Fe. These iron-containing phases have a higher melting point, making them challenging to diffuse evenly during homogenization.

Figure 3a shows the bright-field microstructure image of an Al–Zn–Mg–Cu alloy following homogenization treatment and slow cooling in the furnace. It is observed that the precipitates primarily exhibit a rod-shaped morphology. The rod-shaped precipitates have an approximate diameter of 0.1 μm and a length of around 3 μm . Figure 3b displays the selected area electron diffraction (SAED) image of the region indicated by the red circle. The analysis confirms the presence of the MgZn_2 phase, with a crystallographic band axis of [0221] and the (0112) crystal plane dominating the growth crystal plane. Additionally, Fig. 3d–h depict the element distributions of Al, Zn, Mg, Cu, and Fe,

respectively. The elemental composition of the phase is predominantly composed of Mg, Zn, and Cu elements. Notably, the large-sized flake phase exhibits a higher Cu content than the rod-shaped phase. The bright field microstructure image of the Al–Zn–Mg–Cu alloy is depicted in Fig. 3i. The numerous fine nano-sized phases align with micron-sized precipitates. During the slow cooling process, these two distinct sizes of phases undergo growth. However, during this process, the concentration of Mg and Zn elements in the matrix decreases, and the growth of nucleation sites is insufficient to form nanoscale fine phases [25]. To achieve finer and more dispersed precipitated strengthening phases, generating additional nucleation sites during the nucleation stage is necessary. This generates more competition for growth, leading to mutual inhibition and growth interactions among the precipitated phases. Figure 3j illustrates the

Fig. 2 Distribution of elements in the second phase of aluminum alloy. **a, b, c, d, e, f** The element distributions of Al, Cu, Zn, Mg, and, Fe, respectively



selected area electron diffraction (SAED) image of the yellow circle region. The calibration results indicate the MgZn_2 phase's presence, with a crystal band axis of $[0001]$, and the dominant growth crystal plane is the $(\bar{1}100)$ crystal plane. Figure 3l–p shows the element distributions of Al, Zn, Mg, Cu, and Fe, respectively. The presence of Fe elements in this morphology may contribute to the larger phase diameter than that shown in Fig. 3a. The low diffusion rate of Fe atoms during heat treatment often leads to micro-segregation and coarsening [26].

Figure 4a shows the bright field microstructure image of the Al–Zn–Mg–Cu alloy. It can be found that the larger phase is composed of several mutually superimposed together to form a larger phase. Figure 4c shows the selected diffraction spot of the green circle region. The calibration result is the $\text{Al}_7\text{Cu}_2\text{Fe}$ phase, and the crystal band axis is $[010]$. Figure 4d shows the selected diffraction spot corresponding to the red circle region. The orientation relationship between MgZn_2 phase and $\text{Al}_7\text{Cu}_2\text{Fe}$ phase is described as $(10\bar{1}0) \text{MgZn}_2 \parallel (002) \text{Al}_7\text{Cu}_2\text{Fe}$, and $[10\bar{1}0] \text{MgZn}_2 \parallel [010] \text{Al}_7\text{Cu}_2\text{Fe}$. Figure 4e shows the selected diffraction spot from the yellow circle region. The calibration results indicate the band axis of the MgZn_2 phase is $[10\bar{1}0]$, while the band axis of the Al matrix is $[100]$. The orientation relationship between the MgZn_2 phase and Al is $(10\bar{1}0) \text{MgZn}_2 \parallel (020) \text{Al}$ and $[10\bar{1}0] \text{MgZn}_2 \parallel [100] \text{Al}$. Figure 4f illustrates the element distributions of Zn, Mg, Cu, and Fe, respectively. The element distribution map reveals that the main elements in the phase where the green circle is located are Al, Cu, and Fe, which aligns with the selected diffraction spots and verifies the phase as $\text{Al}_7\text{Cu}_2\text{Fe}$. Additionally, the main elements in the red circle consist of Mg, Zn, and a small amount of Cu. The MgZn_2 phase overlays the iron-containing phase, a structure commonly found at the grain boundary. The precipitated MgZn_2 phase nucleates and grows alongside the iron containing

phase as a heterogeneous point. Previous studies have examined similar structures where this type of precipitate exists at the coarse S or iron phase interface [27, 28].

Figure 4j shows the selected diffraction spot in the yellow circle area. The orientation relationship between the MgZn_2 phase and Al is as follows: $[\bar{1}1\bar{0}0] \text{MgZn}_2 \parallel [110] \text{Al}$, $(1\bar{1}1) \text{Al} \parallel (1122) \text{MgZn}_2$, and $(002) \text{Al} \parallel (0002) \text{MgZn}_2$. Scholars have classified and defined the η phases with different orientation relationships with aluminum in previous studies. These phases have been categorized into a group parallel to the (110) and $(1\bar{1}1)$ Al habit planes. Typically, the (110) Al habit plane phase appears hexagonal or disc shaped. However, cross-section effects may influence this observation, and the rod-like precipitates can be identified as smaller discs. Additionally, previous reports suggest that these different types of MgZn_2 phases can transition from pre-precipitated phases, especially those that exhibit similar orientation relationships [29].

To enhance the strength and toughness of the aluminum alloy, achieving a high density of dispersed nano phases is desired. Kovács conducted research [30] based on theoretical calculations of shear stress for dislocations interacting with and bypassing precipitated particles in an Al–Zn–Mg alloy. The study revealed that while the precipitated phase particles' size was under 6 nm, dislocations cut through the precipitated particles, whereas dislocations generally bypassed the particles when their size exceeded 6 nm. However, while a larger size of the second phase benefits dislocation bypassing, the presence of a large incoherent phase disrupts the matrix continuity and diminishes the alloy's plasticity and toughness [31]. The high density, uniform distribution, and fine η phase particles can make the grain boundary and intra-granular strength of the alloy uniform, which is beneficial to improve the strength and toughness of the alloy synergistically, especially those nano-precipitates with coherent interface relationship with the aluminum matrix [32].

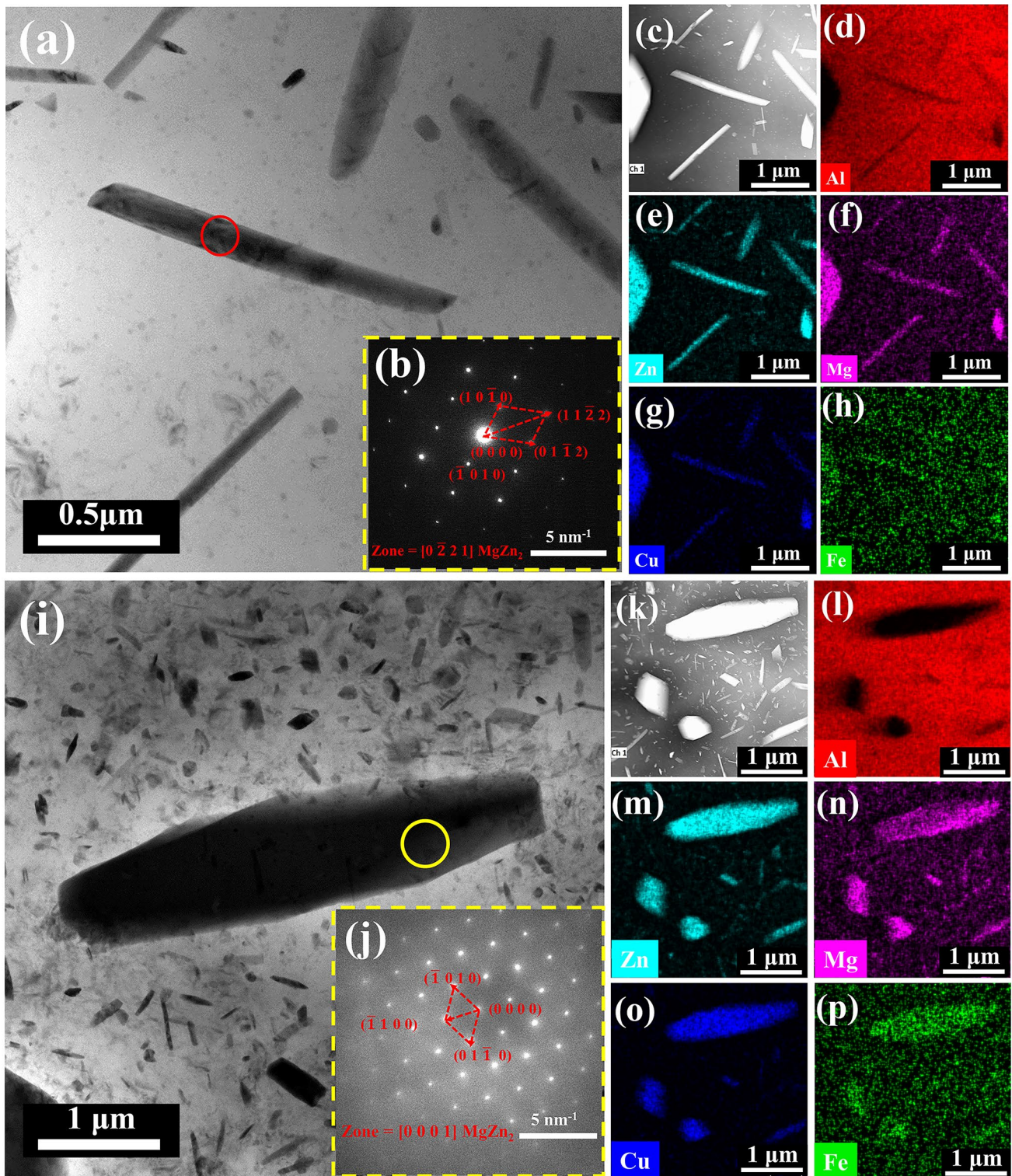


Fig. 3 **a** Microstructure of rod-like second phase. **b** The SAED image in the red circle of Fig. 3a. **c** Microstructure of the EDS region. **d, e, f, g, h** The element distributions of Al, Zn, Mg, Cu, and Fe, respectively. **i** Microstructure of ellipsoidal second phase. **j** The SAED

image in the yellow circle of Fig. 3i. **k** Microstructure of the EDS region. **l, m, n, o, p** The element distributions of Al, Zn, Mg, Cu, and Fe, respectively

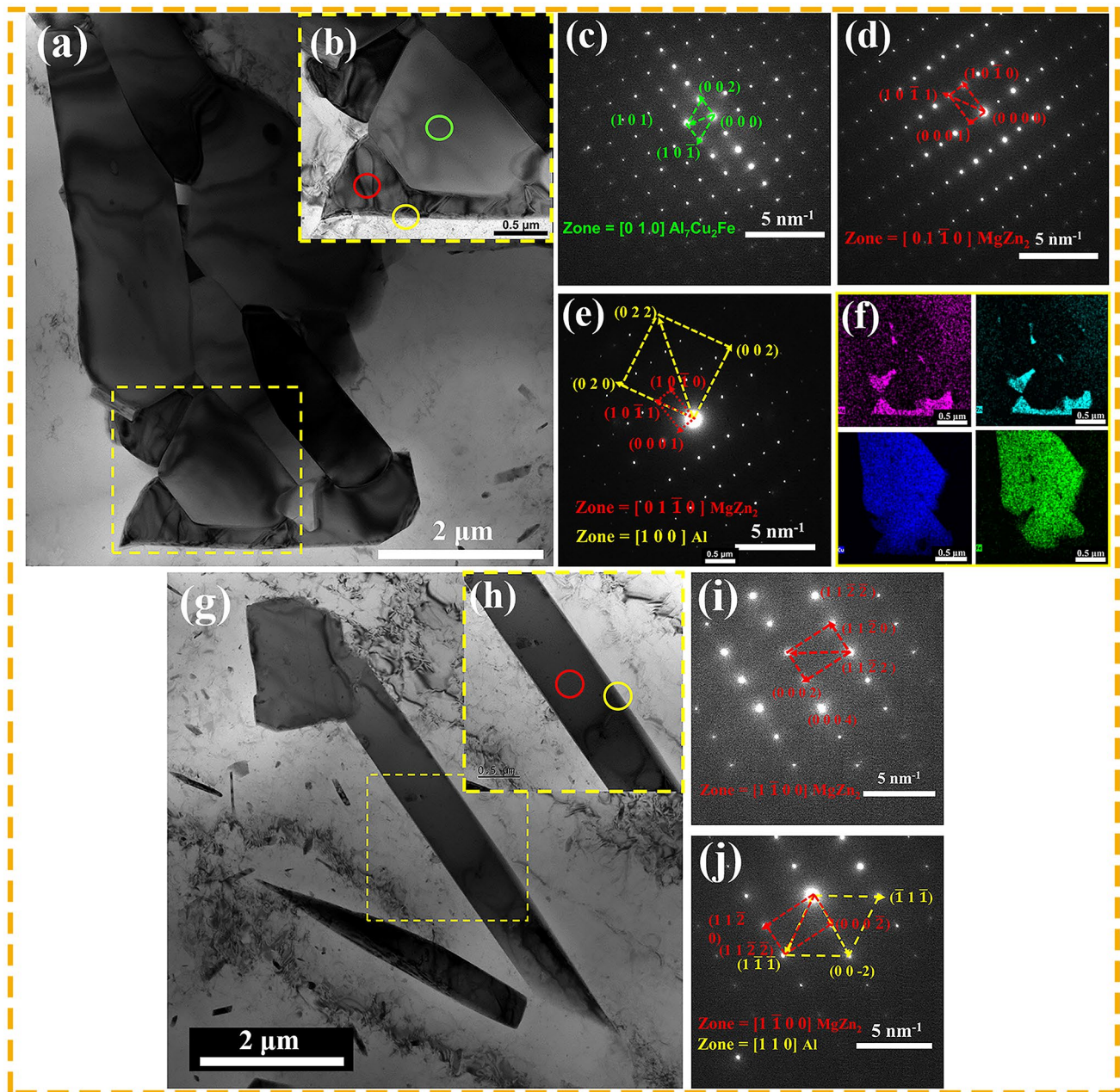


Fig. 4 **a** Microstructure of the second phase. **b** The local enlargement of Fig. 4a. **c** The SAED image in the green circle of Fig. 4b. **d** The SAED image in the red circle of Fig. 4b. **e** The SAED image in the yellow circle of Fig. 4b. **f** The element distributions of Mg, Zn, Cu,

and Fe, respectively. **g** Microstructure of the second phase. **h** The local enlargement of Fig. 4a. **i** The SAED image in the red circle area of Fig. 4h. **j** The SAED image in the yellow circle area of Fig. 4h

Figure S2 shows the line element distribution map and point element diagram of the second phase of Al–Zn–Mg–Cu alloy. The content of Zn, Mg, and Cu elements shows a sharp increase from the matrix interface to the phase, while the content of the Al element decreases to its lowest level. The mass fraction and atomic fraction of Zn and Mg elements are approximately 2:1, by the compositional characteristics of the MgZn₂ phase. The interface exhibits noticeable

fluctuations in peaks, indicating atomic composition variations that affect the arrangement of interface atoms. The strength of the alloy is significantly influenced by the adhesion at the interface [33]. Hence, it is worthwhile to explore the relationship between the arrangement of interface atoms and interface adhesion, as the phase interface is influenced by directionality.

3.3 Evolution of MgZn₂ Phase

To strengthen the alloy, it is crucial to have the MgZn₂ Phase in a fine size and dispersed distribution. To comprehend the evolution of the MgZn₂ Phase during heat treatment, SEM analyzed the alloy's microstructure after subjecting it to various temperatures and durations. Figure 5a, b shows the microstructure after homogenization and slow cooling, which is also the initial microstructure of the subsequent heat treatment sample. The crystal contains numerous

dispersed rod-shaped second phases, ranging from approximately 2 to 10 μm. The microstructure at 460 °C/5 min is depicted in Fig. 5c. A comparison with the initial microstructure reveals that certain smaller MgZn₂ phases dissolve into the matrix. This phenomenon occurs due to the ease of dissolution and activation of the small-sized phase during heating, which facilitates Mg and Zn atom diffusion and dissolution [34]. Dissolution primarily occurs at the grain boundary, as the precipitated phase near the grain boundary accumulates along it, creating a non-precipitation zone of

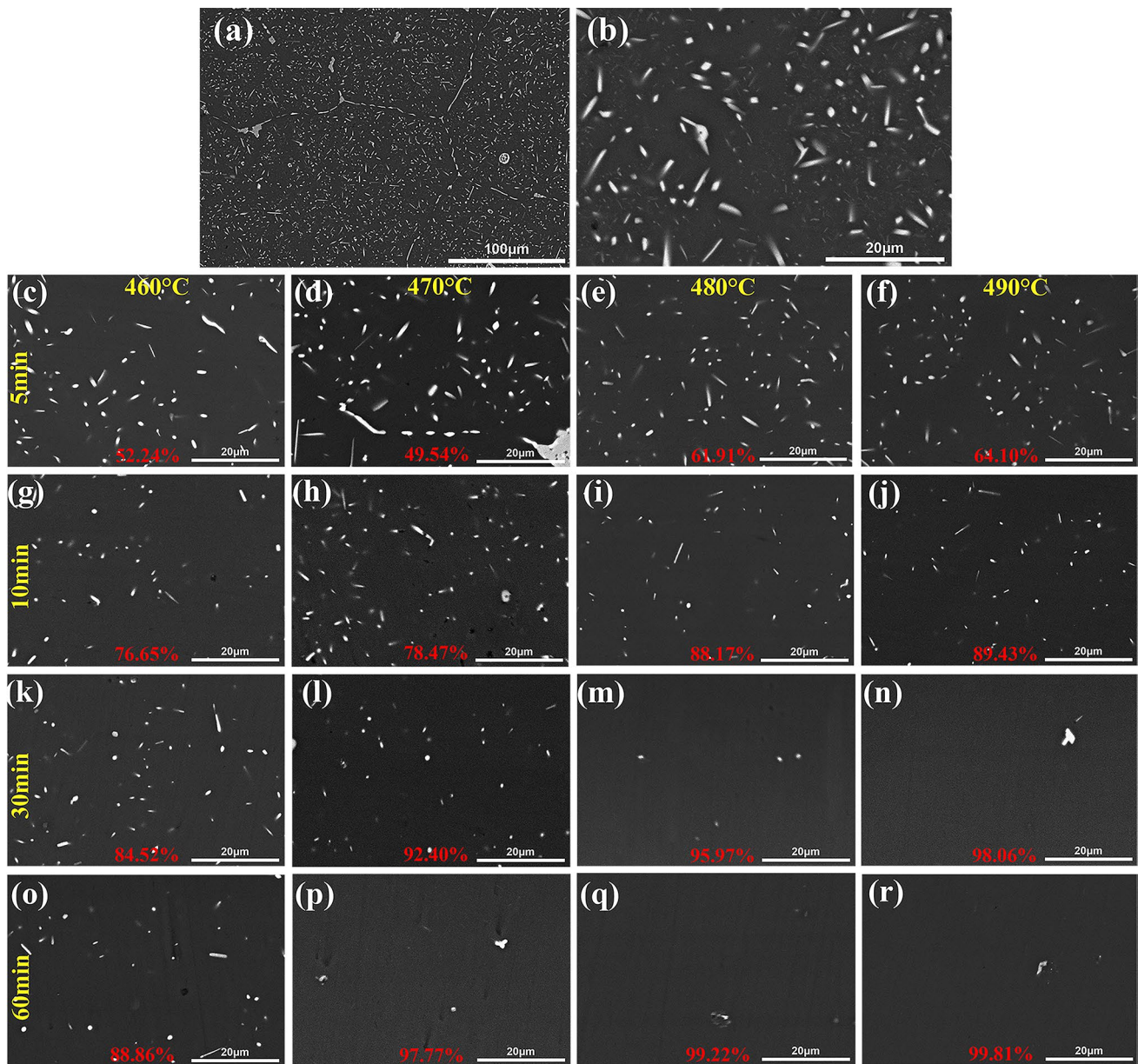


Fig. 5 Microstructure of aluminum alloy different heat treatment processes. **a** Cooling with furnace after homogenization. **b** Magnification diagram of the yellow region. **c** 460 °C/5 min; **d** 470 °C/5 min; **e** 480 °C/5 min; **f** 490 °C/5 min; **g** 460 °C/10 min; **h** 470 °C/10 min; **i** 480

°C/10 min; **j** 490 °C/10 min; **k** 460 °C/30 min; **l** 470 °C/30 min; **m** 480 °C/30 min; **n** 490 °C/30 min; **o** 460 °C/60 min; **p** 470 °C/60 min; **q** 480 °C/60 min; **r** 490 °C/60 min. (The red word in the figure is the dissolution rate of MgZn₂)

approximately 10 μm. Consequently, the concentration of Mg and Zn atoms at the grain boundary is lower, leading to a larger concentration gradient between the phase at the grain boundary and the matrix.

Figure 5g shows the microstructure of 460 °C/10 min. The dissolution of the MgZn₂ Phase becomes more apparent after 10 min at this temperature, resulting in a significant reduction in the density and size of the MgZn₂ Phase compared to 5 min. Figure 5k, o depicts the microstructure after 30 min and 60 min of treatment at 460 °C, respectively. The density of the MgZn₂ phase at these two periods does not significantly differ from that at 10 min, suggesting a deceleration in the dissolution trend after 10 min at this temperature. Furthermore, the low driving force for the diffusion of MgZn₂ atoms at this temperature is evident. At 460 °C, a substantial dissolution of phases occurs within 5–10 min. Subsequently, due to a decrease in the concentration gradient difference between the MgZn₂ atoms and the matrix, leading to a decline in the dissolution rate [35]. Figure 5h, l, p displays the microstructure after 10 min, 30 min, and 60 min of treatment at 470 °C, respectively. The coarse phase at the grain boundary remains undissolved, while the density of the MgZn₂ phase decreases as the holding time increases. Notably, the MgZn₂ phase at 470 °C/60 min undergoes near-complete dissolution into the matrix, with only a small residue remaining undissolved. It shows that the dissolution rate at 470 °C is faster than 460 °C. Particularly after 30 min, the atomic concentration difference between the matrix and the interface decreases, necessitating a stronger driving force for atom diffusion.

Figure 5i and m show the microstructure diagram at 480 °C for 10 min and 30 min, respectively. The density of the MgZn₂ phase decreases at this temperature, and the dissolution rate is faster than 460 °C and 470 °C. It can be seen from the microstructure of 30 min and 60 min that the MgZn₂ phase is almost completely dissolved into the matrix, and the dissolution time is shorter than that at 470 °C. The dissolution process involves atom diffusion, as solid-state diffusion occurs through the thermal activation of atoms. With increasing temperature, atomic vibrations become more intense, increasing the activation probability and thereby reducing the dissolution time [36]. Figure 5j, n shows the microstructure diagram at 490 °C for 10 min and 30 min, respectively. It is found that the microstructure at this temperature is like that at 480 °C. This suggests that the thermal activation effect at 490 °C is not significantly different from that at 480 °C. The limited migration distance of diffusion atoms, less than 1 nm each time, results in the considerable time needed to fully dissolve the second phase and form a solid solution within the matrix lattice [37]. This indicates that the dissolution process is governed by atom diffusion, and the gradual incorporation of the second phase into the matrix lattice is time dependent.

Figure 6a shows the statistical results of the second phase from several micrographs. The initial volume fraction of the second phase conforms to the thermodynamic calculation results. It shows that the thermodynamic calculation results can be well predicted, so it is feasible to customize the experimental scheme with reference to the simulation

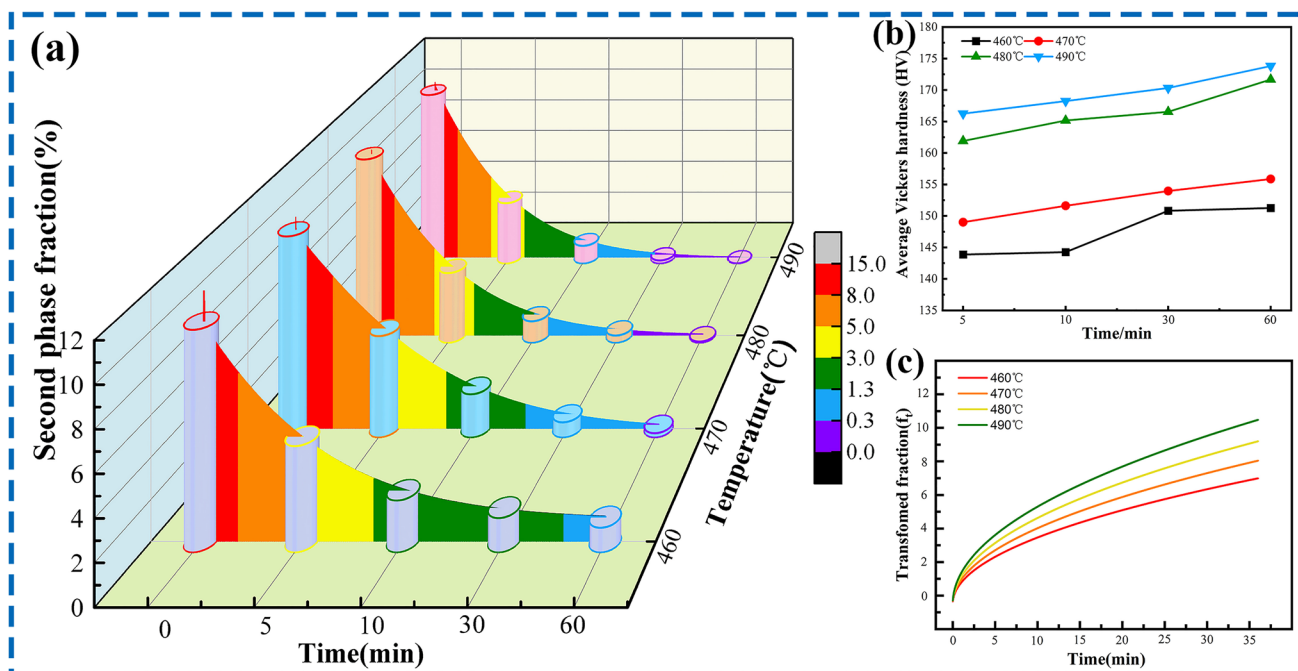


Fig. 6 a MgZn₂ phase content in different heat treatment processes. (Among them, the column is the experimental statistical result, and the curve is the fitting result.) b Micro-hardness of different heat

treatments. c Theoretical model: the evolution relationship between the volume fraction of the second phase transition and time

results. By observing the height of the columns and the distribution of colors in the diagram, a clear trend emerges: the fraction of the second phase decreases with longer treatment times and higher temperatures. These conditions, namely longer treatment times and higher temperatures, facilitate the diffusion of solid metal atoms [38]. In order to provide a more intuitive analysis of the influence of temperature on the diffusion of atoms, an exponential function relationship is utilized to demonstrate the changing pattern between the diffusion coefficient and temperature. Consequently, the calculation equation for the solid diffusion coefficient of Zn, Mg, and Cu elements [39] is derived, and the detailed information is shown in Table 2. The results show that the diffusion coefficient of Zn is 5 times and 3 times larger than Cu and Mg's, respectively. During the heat treatment process, the Zn element at the MgZn₂ phase interface diffuses into the aluminum matrix at a higher diffusion rate, followed by the Mg element. The atomic composition ratio of the MgZn₂ phase closely aligns with a 1:2 ratio, resembling the diffusion rate ratio of Mg and Zn atoms. This relationship may be attributed to the composition of the MgZn₂ phase and has implications for the balance of atomic precipitation and dissolution processes. With increasing temperature, the diffusion rate also rises, causing the gap in diffusion rates between Zn and Mg, and Cu to gradually diminish. This observation suggests a higher dissolution efficiency during the high-temperature stage.

3.4 Vickers hardness

Figure 6b illustrates the Vickers hardness of the sample following heat treatment at various temperatures and durations. The figure reveals that the Vickers hardness of the aluminum alloy increases with longer treatment times at each temperature while also showing an increase in Vickers hardness with higher treatment temperatures. In general, elevating the temperature or extending the duration promotes a more extensive dissolution of the undissolved second phase into the matrix, resulting in a higher degree of super-saturation of alloying elements. The presence of solid solution atoms in the lattice leads to lattice distortion, with greater distortion occurring as the radius difference between solute atoms and solvent atoms increases [41, 42]. As the second phase dissolves,

solute atoms fully diffuse into the aluminum matrix, resulting in increased lattice distortion and a stronger strengthening effect. As the temperature increases, the driving force for phase transformation intensifies, leading to a sharp increase in the atomic diffusion coefficient. Consequently, the second phase dissolves and diffuses more comprehensively. Additionally, higher temperatures promote the generation of more vacancies, enabling more solute atoms to dissolve into the aluminum matrix and induce increased lattice distortion [43].

Additionally, the disparity in size between solute atoms and solvent atoms influences the degree of lattice distortion. The radii of aluminum, zinc, magnesium, and copper atoms are 1.43, 1.39, 1.60, and 1.28 Å, respectively. The relative size of the solute atom and the solvent atom is calculated by Eq. (1), resulting in $\Delta r_{\text{Al-Mg}} = 0.1189$, $\Delta r_{\text{Al-Zn}} = 0.0279$, and $\Delta r_{\text{Al-Cu}} = 0.1049$. The comparison reveals that the relative size between Al-Mg and Al-Cu components is similar, whereas the relative size between Al-Zn components is smaller. This suggests that the lattice distortion caused by the dissolution of Mg and Cu atoms is significantly larger than that caused by Zn atoms. During the initial stages at low temperatures, Mg and Zn atoms enter the MgZn₂ phase of the matrix and dissolve first. As the temperature rises, the Al₂CuMg phase dissolves, resulting in a significant amount of Cu and Mg atoms being dissolved into the matrix and generating substantial lattice distortion.

Figure 6b can be seen that the Vickers hardness at 480 °C and 490 °C is significantly higher than that at 460 °C and 470 °C, which also indicates that more solute atoms begin to enter the matrix at 480 °C, which is likely to be the dissolution of the Al₂CuMg phase with a higher melting point [44]. The introduction of Cu and Mg atoms into the matrix results in an increase in solute atoms within the matrix. This, coupled with the influence of the size difference between Mg, Cu, and Al atoms, significantly enhances the strengthening effect. Moreover, solution treatment facilitates the dissolution of second phase particles into the matrix, subsequently decomposing into nano-sized precipitates (GP zone or η' -phase) by using natural aging (NA) and artificial aging (AA), leading to significant aging hardening [45]. While the experimental alloy did not undergo aging heat treatment, it is worth considering the influence of natural aging. The higher the degree of dissolution, following the

Table 2 Solid diffusion coefficient (D) of Cu, Mg, and Zn elements during heat treatment (m²·s⁻¹)

Elements	Calculated equation [40]	D ₀	460 °C	470 °C	480 °C	490 °C
Cu	$D = D_0 \exp(-16,069/T)$	4.8×10^{-5}	1.454×10^{-14}	1.952×10^{-14}	2.602×10^{-14}	3.441×10^{-14}
Mg	$D = D_0 \exp(-13,831/T)$	6.23×10^{-6}	3.994×10^{-14}	5.149×10^{-14}	6.592×10^{-14}	8.385×10^{-14}
Zn	$D = D_0 \exp(-14,385/T)$	2.45×10^{-5}	7.378×10^{-14}	9.608×10^{-14}	1.242×10^{-13}	1.596×10^{-13}
D _{Cu} : D _{Mg} : D _{Zn}	/	/	1.0:2.7:5.1	1.0:2.6:4.9	1.0:2.5:4.8	1.0:2.4:4.5

formation of a supersaturated solid solution in the matrix, the stronger the driving force for precipitation, leading to denser and smaller-sized precipitates. Apart from solid solution strengthening, there is a proportionate contribution of precipitation strengthening [46].

$$\Delta r = \left| \frac{r_a - r_b}{r_a} \right| \tag{1}$$

where Δr is the relative size of solute and solvent atoms; r_a is the atomic size of the solvent, and r_b is the size of solute atom.

3.5 MgZn₂ phase dissolution kinetics

To investigate the dissolution behavior of MgZn₂, the influence of solute diffusion in the system was analyzed using the classical Johnson–Mehl–Avrami (JMA) theoretical framework. Before establishing the kinetic dissolution model, the transition fraction f was introduced [47].

$$f_t = (p - p_0)/(p_e - p_0) 0 \leq f_t \leq 1 \tag{2}$$

Here, p is a physical quantity that change with the transition process; p_0 is the value corresponding to the initial transition state p ; p_e is the value corresponding to the final state p .

The dissolution of the second phase, f_t can be expressed as follows:

$$f_t = \frac{f - f_0}{f_e - f_0} \tag{3}$$

Here, f is the volume fraction of the second phase in the dissolution process; f_0 is the initial volume fraction of the second phase; f_e is the volume fraction of the second phase after transformation.

The evolution of the transition fraction with time in particle systems is analyzed based on the Johnson–Mehl–Avrami (JMA) theoretical framework, and the associated kinetic parameters are suitably adjusted [48]:

$$f_t = 1 - \exp(-x_t) \tag{4}$$

where x_t is the extended transition fraction, $x_t = (Wt)^n$,

$$f = f_e + (f_0 - f_e) \exp(-(Wt)^n) \tag{5}$$

The experimental results are used to substitute into Eq. (5), with n and W being fitted as parameters. The resulting equation can be utilized to describe the actual dissolution process [49]. The model parameters fitted by experimental data are listed in Table 3. Through the fitted R^2 value, the simulation parameters fit well. The MgZn₂ phase fitting curve is shown in Fig. 6a. This demonstrates that the fitted model effectively predicts the content of the second

Table 3 Model fitting parameters

Temperature (°C)	f_e	f_0	W	n	R^2
460	1.060	18.585	0.688 ± 0.10	1.266 ± 0.23	0.9998
470	0.100	15.433	0.524 ± 0.01	1.461 ± 0.07	0.9999
480	0.030	19.737	0.713 ± 0.06	1.338 ± 0.14	0.9999
490	0	22.213	0.767 ± 0.08	1.333 ± 0.17	0.9999

phase, enabling the calculation of the second phase content at a specific temperature and time, facilitating regulation of the desired phase content. However, the equation is only an empirical model of the rough deformation of the classical JMA theory, and the parameters in the equation have no specific physical meaning because this is a microscopic theory that does not consider diffusion in the dissolution process [50]. To make the model more consistent with the solute diffusion process in the dissolution process, the extended transition fraction in the model is based on the solute diffusion behavior, and the dissolution kinetic model is obtained from both experimental data and theoretical derivation.

The most commonly used kinetic dissolution model of bulk diffusion control is shown in Eq. (6) [51].

$$\frac{dR}{dt} = -\frac{K}{2} \left(\frac{D}{R} + \sqrt{\frac{D}{\pi t}} \right) \tag{6}$$

Here, R is the second phase radius; t is the dissolution time; K is the shape factor; D is the atomic diffusion coefficient.

$$K = 2 \frac{C_\alpha - C_M}{C_\beta - C_\alpha} \tag{7}$$

Here, C_α is the atomic concentration at the interface between the second phase and the matrix; C_M is the concentration of atoms in the matrix; C_β is the concentration of atoms in the second phase.

$$\frac{dR}{dt} = -\frac{C_\alpha - C_M}{C_\beta - C_\alpha} \left(\frac{D}{R} + \sqrt{\frac{D}{\pi t}} \right) \tag{8}$$

At present, the most used dissolution kinetic model controlled by volume diffusion characterizes the diffusion of the spherical model phase. This study aims at the dissolution of the MgZn₂ phase, and the morphology of the MgZn₂ phase is a round rod. It is necessary to modify its shape when using this model and introduce volume change correction to the expansion fraction. The specific content of volume change correction is shown in support information.

Figure 6c shows the evolving relationship between the volume fraction of the second phase transition and time

during heat treatment using this model. The theoretical results agree with the overall trend of the experimental data. The dissolution of the η (MgZn_2) phase is essentially the diffusion of Mg and Zn atoms. The diffusion coefficients of Mg and Zn atoms in the aluminum matrix are calculated from Table 2. Since the number of Zn atoms in the η (MgZn_2) phase dissolution system is close to twice that of mg atoms, the diffusion rate of Zn atoms is used as the dissolution rate of the η (MgZn_2) phase. According to the Mg-Zn binary phase diagram, the mass fraction of Zn atoms around the η phase interface in the matrix is $C_\alpha \approx 0.43$. The alloy's mass fraction of the Zn atom in η phase is $C_\beta = 0.84$.

From Table 1, the alloy's mass fraction of the Zn atom is $C_M = 0.064$. When subjected to the same heat treatment time, a higher temperature results in a greater extent of second phase dissolution, with the difference increasing over time.

3.6 Microscopic characterization of phase interface

To better understand the solubility of the MgZn_2 phase and the mechanism of its influence on the alloy from a microscopic perspective, HRTEM characterization Al/ MgZn_2 interface. The Al/ MgZn_2 interface orientation relationship largely determines the interface bonding strength and is also a key

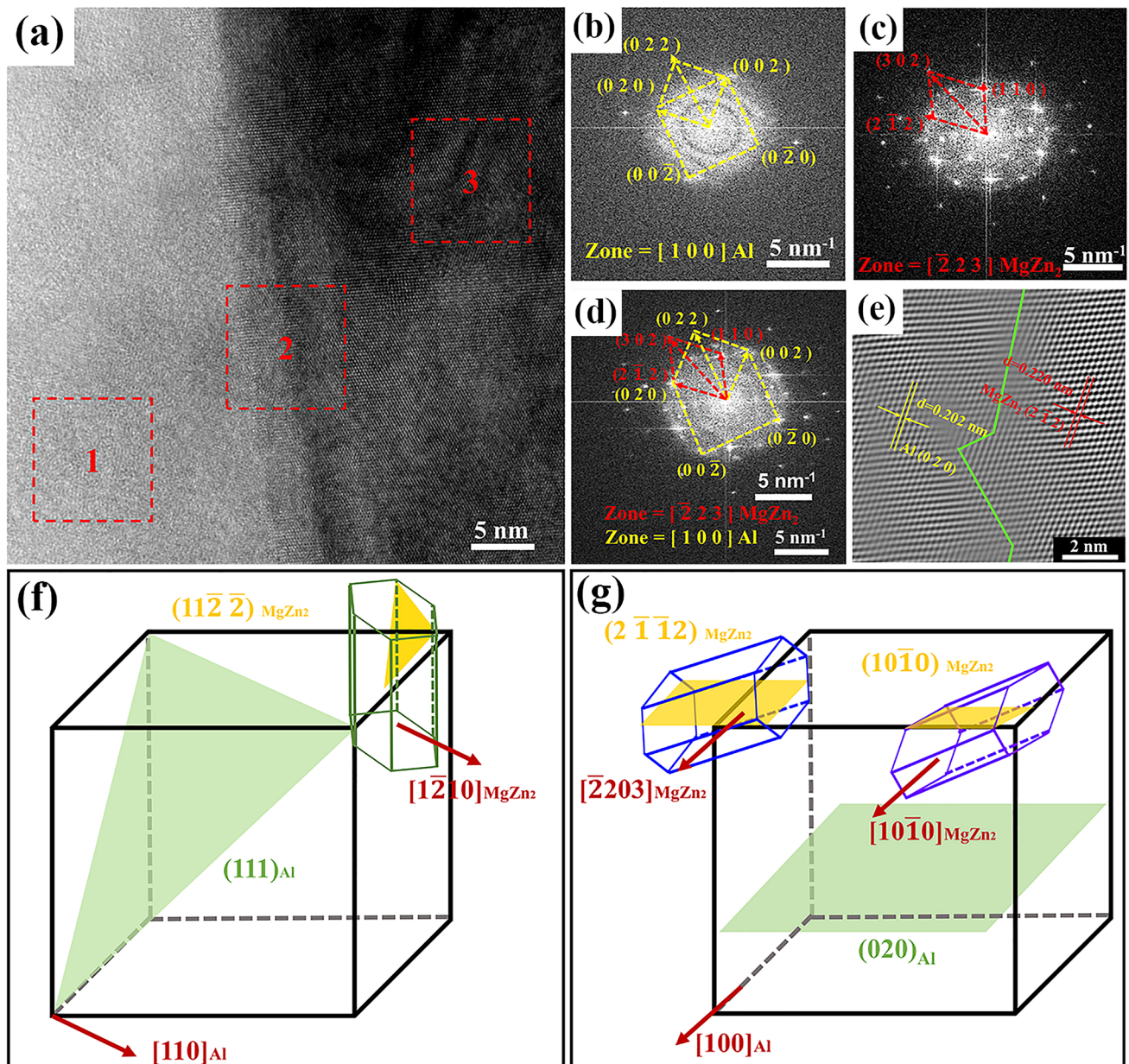


Fig. 7 a Microscopic morphology of Al/ MgZn_2 interface. b The FFT of zone 1 in a; c the FFT of zone 3 in a; d the FFT of zone 2 in a; e the IFFT for zone 2 in a. The schematic illustration that indicates the

morphologies of varying kinds of η precipitates and their orientation relationships being concerned with the Al crystal: f $[110]_{\text{Al}}$; g $[100]_{\text{Al}}$

factor in studying the diffusion of Mg and Zn atoms at the interface. Figure 7a shows the microscopic morphology and interfacial orientation relationships of Al/MgZn₂ interface. In the figure, the white and bright area on the left is the Al matrix and the dark area on the right is MgZn₂. The phase interface of the transition region can be seen between the matrix and the phase. Figure 7b shows the FFT of zone 1. The calibration result is Al and the crystal band axis is [100]. Figure 7c shows the FFT of zone 3. The calibration result is MgZn₂ and the crystal band axis is $[\bar{2}23]$. Figure 7d shows the FFT of zone 2, which is the interface region between the Al matrix and phase. The SAED in Fig. 7d indicates that the [100] Al zone axis of Al is parallel to the incident electron beam, whereas the $[\bar{2}23]$ MgZn₂ zone axis of MgZn₂ is parallel to the incident electron beam, so there is $[\bar{2}23]$ MgZn₂||[100] Al. Meanwhile, $(\bar{2}\bar{1}2)$ MgZn₂|| (020) Al is known from Fig. 7d shows the orientation relationships of MgZn₂/Al interface are $[\bar{2}\bar{1}2]$ MgZn₂|| (020) Al, $[\bar{2}23]$ MgZn₂||[100] Al. Figure 7e shows the IFFT for zone 2. The interplanar spacing of (020) Al is 0.202 nm, while that of $(\bar{2}\bar{1}2)$ MgZn₂ is 0.220 nm, indicating a distance proximity between these two parallel crystal planes.

From the microscopic picture, it can be found that there is lattice distortion in the two phases interface bonding. In general, the twisted interface structure has large defects and interface energy, which provides diffusion channels and potential energy conditions for interface atom diffusion. The mismatch configuration of atoms at the interface cannot be simply understood as an interface defect but as a necessary condition for stabilizing the interface [52]. The high defect concentration at the interface facilitates the diffusion of Mg and Zn atoms. Therefore is requisite to comprehensively consider the diffusion behavior of interface atoms to study the dissolution and growth of the MgZn₂ phase.

Figure 7f and g shows a schematic diagram depicting the morphologies of different orientation relationships and η precipitates concerning the Al crystal. Figure 7f shows the orientation relationship between MgZn₂ phase and Al are $[1\bar{1}00]$ MgZn₂ || $[\bar{1}10]$ Al, (111) Al || (1122) MgZn₂. Figure 7g shows the orientation relationship between MgZn₂ phase and Al is $(10\bar{1}1)$ MgZn₂ || (020) Al and $[01\bar{1}0]$ MgZn₂ || $[100]$ Al. The orientation relationship between MgZn₂ phase and Al matrix is $[\bar{2}23]$ MgZn₂ || $[100]$ Al and $(\bar{2}\bar{1}2)$ MgZn₂ || (020) Al. The lower interface energy resulting from a lower lattice mismatch during the growth of the precipitated MgZn₂ phase plays a crucial role in determining the growth direction and resulting morphologies. The influence of morphology on [53] is also an important factor in the dissolution process. Certainly, the arrangement of atoms at the interface and the lattice distortion at the interface will affect the diffusion path of atoms. Therefore, in the subsequent research, we will consider the influence of the second phase interface structure on the specific dissolution behavior, and deeply understand the contribution of the second phase interface structure in the strengthening alloy and its strengthening mechanism.

4 Conclusion

The dissolution behavior of MgZn₂ phase during heat treatment was studied by changing the heat treatment temperature and time in the article. The following conclusions have been drawn.

The calculation results show that the η (MgZn₂) weight fraction of Al–Zn–Mg–Cu alloy is 9.12% at room temperature, which accords with the experimental results. Additionally, the critical cooling rates for the GP zone and η (MgZn₂) are determined to be 0.69 and 166.6 °C/s, respectively.

Temperature and time are primary factors that influence the dissolution of the MgZn₂ phase. With the increase in temperature and time, the dissolution degree of MgZn₂ phase is higher. The dissolution rates of MgZn₂ phase at 460 °C/60 min, 480 °C/60 min and 490 °C/60 min were 88.86%, 99.22%, and 99.81%, respectively. More dissolution corresponds to a higher degree of super-saturation of the alloy solute, leading to increased hardness.

Based on the statistical data of the experimental alloy MgZn₂ phase, the semi-empirical dissolution model was fitted based on the JMA theoretical model to describe the relationship between the volume fraction of MgZn₂ phase and time under isothermal heat treatment. Based on the classical dissolution model and JMA theory, an analytical model of solute diffusion including the front of the second phase/Al matrix interface is established.

Supplementary Information The online version contains supplementary material available at <https://doi.org/10.1007/s42114-023-00785-3>.

Author contribution Shanju Zheng, Xiaohong Yuan, and Xiaojing Wang conceived and supervised the research. Hongfu Yang, Yelin Zhang, Rensong Huang, Shumeng Lu, and Peng Sun carried out the materials preparation. Hongfu Yang, Yelin Zhang, Rensong Huang, and Xiaohong Yuan performed sample characterization and sensor test. Hongfu Yang, Yelin Zhang, Shanju Zheng, and Mengnie Li, analyzed data and wrote the manuscript. Zaki I. Zaki, Mohamed M. Ibrahim, Hua Hou, and Zeinhom M. El-Bahy polished and reviewed the language. All authors participated in discussion, revision, and approval of the manuscript.

Funding This work was financially supported by the Key Research & Development Program of Yunnan Province (Grant numbers 202103AA080017, CBN21281004A and 202203AE140011), The Yunnan Ten Thousand Talents Plan Young & Elite Talents Project (Grant number YNWR-QNBJ-2020-020), The Yunnan Fundamental Research Projects (Grant No. 202101AU070152), The Natural Science Research Foundation of Kunming University of Science and Technology (Grant number KKZ3202051043), and Chuoli Chengcai Training Program of KUST Faculty of Materials Science and Engineering (CLXYCLCC20230701). The researchers would like to acknowledge Deanship of Scientific Research, Taif University for funding this work.

Data availability The raw/processed data needed to reproduce these findings cannot be shared at this time as the data also forms part of an ongoing study.

Declarations

Competing interests The authors declare no competing interests.

References

- Marlaud T, Deschamps A, Bley F, Lefebvre W, Baroux B (2010) Evolution of precipitate microstructures during the retrogression and re-ageing heat treatment of an Al–Zn–Mg–Cu alloy. *Acta Mater* 58:4814–4826. <https://doi.org/10.1016/j.actamat.2010.05.017>
- Azarniya A, Taheri AK, Taheri KK (2019) Recent advances in ageing of 7xxx series aluminum alloys: a physical metallurgy perspective. *J Alloys Compd* 781:945–983. <https://doi.org/10.1016/j.jallcom.2018.11.286>
- Mulky L, Rao P (2023) Effect of operational parameters on fouling of 6061 aluminum alloy under dynamic conditions. *ES Mater Manuf* Volume 21 September 2023:893. <https://doi.org/10.30919/esmm893>
- Huang R, Yang H, Wan L, Zheng S, Li M, Koppala S (2023) Effect of homogenization process on microstructure of Al–Zn–Mg–Cu aluminum alloys. *Adv Eng Mater* 25:2201854. <https://doi.org/10.1002/adem.202201854>
- Sun P, Yang H, Huang R, Zhang Y, Zheng S, Li M, Koppala S (2023) The effect of rolling temperature on the microstructure and properties of multi pass rolled 7A04 aluminum alloy. *J Mater Res Technol* 25:3200–3211. <https://doi.org/10.1016/j.jmrt.2023.06.123>
- Zhao Y (2023) Understanding and design of metallic alloys guided by phase-field simulations. *Npj Comput Mater* 9:1–25. <https://doi.org/10.1038/s41524-023-01038-z>
- Xin T, Zhao Y, Mahjoub R, Jiang J, Yadav A, Nomoto K, Niu R, Tang S, Ji F, Quadir Z, Miskovic D, Daniels J, Xu W, Liao X, Chen L-Q, Hagihara K, Li X, Ringer S, Ferry M (2021) Ultrahigh specific strength in a magnesium alloy strengthened by spinodal decomposition. *Sci Adv* 7:eabf3039. <https://doi.org/10.1126/sciadv.abf3039>
- Ashok A, Desai AS, Mahadeva R, Patole SP, P B, ey, Bhagat N (2023) Research network analysis and machine learning on heusler alloys. *Eng Sci* 25:954. <https://doi.org/10.30919/es954>
- Mao R, Xiang D (2023) Enhancement of mechanical properties of tungsten alloy via disordered microstructure and solid solution strengthening. *Mater Des* 225:111468. <https://doi.org/10.1016/j.matdes.2022.111468>
- Sandeep Nambiar S, eep Nambiar S, Brn Murthy, Sathyashankara Sharma, A. A. Prasanna, Arout Chelvane J (2022) Microstructure and mechanical properties of annealed quinary Ni–Mn–Sn–Fe–In heusler alloy. *Eng Sci* 17:303–308. <https://doi.org/10.30919/es8d632>
- Matsuda K, Kawai A, Watanabe K, Lee S, Marioara CD, Wenner S, Nishimura K, Matsuzaki T, Nunomura N, Sato T, Holmestad R, Ikeno S (2017) Extra electron diffraction spots caused by fine precipitates formed at the early stage of aging in Al–Mg–X (X=Si, Ge, Zn)–Cu alloys. *Mater Trans* 58:167–175. <https://doi.org/10.2320/matertrans.L-M2016839>
- Hansen V, Karlsen OB, Langsrud Y, Gjønnes J (2004) Precipitates, zones and transitions during aging of Al–Zn–Mg–Zr 7000 series alloy. *Mater Sci Technol* 20:185–193. <https://doi.org/10.1179/026708304225010424>
- Komura Y, Tokunaga K (1980) Structural studies of stacking variants in Mg–base friauf–laves phases. *Acta Crystallogr B* 36:1548–1554. <https://doi.org/10.1107/S0567740880006565>
- Priya P, Johnson DR, Krane MJM (2017) Precipitation during cooling of 7xxx aluminum alloys. *Comput Mater Sci* 139:273–284. <https://doi.org/10.1016/j.commatsci.2017.08.008>
- Yang W, Ji S, Wang M, Li Z (2014) Precipitation behaviour of Al–Zn–Mg–Cu alloy and diffraction analysis from η' precipitates in four variants. *J Alloys Compd* 610:623–629. <https://doi.org/10.1016/j.jallcom.2014.05.061>
- Fushun X, Xiaobin G, Pengfei W, Jin Z, Yunlai D (2017) Morphology development and kinetics of plate or rod shaped precipitates in aluminum alloys. *Rare Met Mater Eng* 46:876–881. [https://doi.org/10.1016/S1875-5372\(17\)30115-7](https://doi.org/10.1016/S1875-5372(17)30115-7)
- Kang L, Cui YJ, Zhao G, Tian N (2017) Precipitation kinetics analysis of the cooling process following the solid solution treatment of 7B50 aluminum alloy. *Mater Sci Forum* 898:213–222. <https://doi.org/10.4028/www.scientific.net/MSF.898.213>
- Kongthep J, Juijerm P (2014) Kinetics of precipitation hardening phase in aluminium alloy AA 6110. *Mater Sci Technol* 30:1815–1819. <https://doi.org/10.1179/1743284713Y.0000000488>
- Zhao Y, Liu K, Zhang H, Tian X, Jiang Q, Murugadoss V, Hou H (2022) Dislocation motion in plastic deformation of nano polycrystalline metal materials: a phase field crystal method study. *Adv Compos Hybrid Mater* 5:2546–2556. <https://doi.org/10.1007/s42114-022-00522-2>
- Whelan MJ (2013) On the kinetics of precipitate dissolution. *Met Sci J* 3:95–97. <https://doi.org/10.1179/msc.1969.3.1.95>
- Sha G, Cerezo A (2004) Early-stage precipitation in Al–Zn–Mg–Cu alloy (7050). *Acta Mater* 52:4503–4516. <https://doi.org/10.1016/j.actamat.2004.06.025>
- Liu SD, Yuan YB, Li CB, You JH, Zhang XM (2012) Influence of cooling rate after homogenization on microstructure and mechanical properties of aluminum alloy 7050. *Met Mater Int* 18:679–683. <https://doi.org/10.1007/s12540-012-4016-9>
- Huang Y, Zhang C, Ma Y, Liu Y (2020) Effects of homogenization on the dissolution and precipitation behaviors of intermetallic phase for a Zr and Er containing Al–Zn–Mg–Cu alloy. *Prog Nat Sci Mater Int* 30:47–53. <https://doi.org/10.1016/j.pnsc.2019.12.002>
- Jiang F, Zurob HS, Purdy GR, Wang X, Zhang H (2018) Characterization of the isothermal precipitation kinetics of an Al–Zn–Mg–Cu alloy. *Metall Mater Trans A* 49:5157–5168. <https://doi.org/10.1007/s11661-018-4822-x>
- Ghosh A, Ghosh M, Kalsar R (2019) Influence of homogenisation time on evolution of eutectic phases, dispersoid behaviour and crystallographic texture for Al–Zn–Mg–Cu–Ag alloy. *J Alloys Compd* 802:276–289. <https://doi.org/10.1016/j.jallcom.2019.06.091>
- Li Y, Deng Y, Fan S, Guo X, Jiang K, Zhang Z, Sun L (2020) An in-situ study on the dissolution of intermetallic compounds in the Al–Zn–Mg–Cu alloy. *J Alloys Compd* 829:154612. <https://doi.org/10.1016/j.jallcom.2020.154612>
- Sirichaivetkul R, Wongpinij T, Euaruksakul C, Limmaneevichitr C, Kajornchaiyakul J (2019) In-situ study of microstructural evolution during thermal treatment of 6063 aluminum alloy. *Mater Lett* 250:42–45. <https://doi.org/10.1016/j.matlet.2019.04.120>
- Bayat N, Carlberg T, Cieslar M (2017) In-situ study of phase transformations during homogenization of 6005 and 6082 Al alloys. *J Alloys Compd* 725:504–509. <https://doi.org/10.1016/j.jallcom.2017.07.149>
- Bendo A, Matsuda K, Lee S, Nishimura K, Nunomura N, Toda H, Yamaguchi M, Tsuru T, Hirayama K, Shimizu K, Gao H, Ebihara K, Itakura M, Yoshida T, Murakami S (2018) Atomic scale HAADF-STEM study of η' and η_1 phases in peak-aged Al–Zn–Mg alloys. *J Mater Sci* 53:4598–4611. <https://doi.org/10.1007/s10853-017-1873-0>
- Kovács I, Lendvai J, Ungar T, Groma G, Lakner J (1980) Mechanical properties of Al–Zn–Mg alloys. *Acta Metall* 28:1621–1631. [https://doi.org/10.1016/0001-6160\(80\)90015-2](https://doi.org/10.1016/0001-6160(80)90015-2)
- Liu D, Xiong B, Bian F, Li Z, Li X, Zhang Y, Wang Q, Xie G, Wang F, Liu H (2015) Quantitative study of nanoscale precipitates in Al–Zn–Mg–Cu alloys with different chemical compositions.

- Mater Sci Eng A 639:245–251. <https://doi.org/10.1016/j.msea.2015.04.104>
32. Tian N, Jiang X, Zhang Y, Zeng Z, Wang T, Zhao G, Qin G (2022) Effect of precipitates on the mechanical performance of 7005 aluminum alloy plates. *Materials* 15:5951. <https://doi.org/10.3390/ma15175951>
 33. Cao F, Zheng J, Jiang Y, Chen B, Wang Y, Hu T (2019) Experimental and DFT characterization of η' nano-phase and its interfaces in Al–Zn–Mg–Cu alloys. *Acta Mater* 164:207–219. <https://doi.org/10.1016/j.actamat.2018.10.045>
 34. Guo F-B, Zhu B-H, Jin L-B, Wang G-J, Yan H-W, Li Z-H, Zhang Y-A, Xiong B-Q (2021) Microstructure and mechanical properties of 7A56 aluminum alloy after solution treatment. *Rare Met* 40:168–175. <https://doi.org/10.1007/s12598-017-0985-7>
 35. Zou X, Yan H, Chen X (2017) Evolution of second phases and mechanical properties of 7075 Al alloy processed by solution heat treatment. *Trans Nonferrous Met Soc China* 27:2146–2155. [https://doi.org/10.1016/S1003-6326\(17\)60240-1](https://doi.org/10.1016/S1003-6326(17)60240-1)
 36. Milkereit B, Österreich M, Schuster P, Kirov G, Mukeli E, Kessler O (2018) Dissolution and precipitation behavior for hot forming of 7021 and 7075 aluminum alloys. *Metals* 8:531. <https://doi.org/10.3390/met8070531>
 37. Xie Y, Liu S, Deng Y, Guo X (2023) Improving the strength contribution of T1 precipitates in Al-4Cu-1.2Li-0.1Sc alloys by dissolving Cu-enriched second phases. *Mater Charact* 198:112751. <https://doi.org/10.1016/j.matchar.2023.112751>
 38. Du Y, Zhang L, Cui S, Zhao D, Liu D, Zhang W, Sun W, Jie W (2012) Atomic mobilities and diffusivities in Al alloys. *Sci China Technol Sci* 55:306–328. <https://doi.org/10.1007/s11431-011-4692-6>
 39. Xie F, Yan X, Ding L, Zhang F, Chen S, Chu MG, Chang YA (2003) A study of microstructure and microsegregation of aluminum 7050 alloy. *Mater Sci Eng A* 355:144–153. [https://doi.org/10.1016/S0921-5093\(03\)00056-X](https://doi.org/10.1016/S0921-5093(03)00056-X)
 40. Wen K, Xiong B-Q, Fan Y-Q, Zhang Y-A, Li Z-H, Li X-W, Wang F, Liu H-W (2018) Transformation and dissolution of second phases during solution treatment of an Al–Zn–Mg–Cu alloy containing high zinc. *Rare Met* 37:376–380. <https://doi.org/10.1007/s12598-016-0768-6>
 41. Zhang X, Chen T (2020) Bimodal microstructure dispersed with nanosized precipitates makes strong aluminum alloy with large ductility. *Mater Des* 191:108695. <https://doi.org/10.1016/j.matdes.2020.108695>
 42. Wang Z, Fang Q, Li J, Liu B, Liu Y (2018) Effect of lattice distortion on solid solution strengthening of BCC high-entropy alloys. *J Mater Sci Technol* 34:349–354. <https://doi.org/10.1016/j.jmst.2017.07.013>
 43. Liu J, Du Z, Su J, Tang J, Jiang F, Fu D, Teng J, Zhang H (2023) Effect of quenching residual stress on precipitation behaviour of 7085 aluminium alloy. *J Mater Sci Technol* 132:154–165. <https://doi.org/10.1016/j.jmst.2022.06.010>
 44. Liang M, Chen L, Zhao G, Guo Y (2020) Effects of solution treatment on the microstructure and mechanical properties of naturally aged EN AW 2024 Al alloy sheet. *J Alloys Compd* 824:153943. <https://doi.org/10.1016/j.jallcom.2020.153943>
 45. Meng X, Zhang D, Zhang W, Qiu C, Liang G, Chen J (2021) Influence of solution treatment on microstructures and mechanical properties of a naturally-aged Al-27Zn-1.5Mg-1.2Cu-0.08Zr aluminum alloy. *Mater Sci Eng A* 802:140623. <https://doi.org/10.1016/j.msea.2020.140623>
 46. Lin M, Yang Z, Shi X, Chen Y, Lu J, Wang Z, Li J, Wang J, He F (2023) Effective combination of solid solution strengthening and precipitation hardening in Ni-Cr-Fe-W-Ti-Al multi-principal element alloys. *J Alloys Compd* 933:167738. <https://doi.org/10.1016/j.jallcom.2022.167738>
 47. Mittemeijer EJ (1992) Analysis of the kinetics of phase transformations. *J Mater Sci* 27:3977–3987. <https://doi.org/10.1007/BF01105093>
 48. Trujillo MP, Orozco A, Casas-Ruiz M, Liger RA, Jimenez-Garay R (1995) Crystallization kinetics study of Fe-B-Si metallic glasses in the theoretical frame of the JMA model. *Mater Lett* 24:287–290. [https://doi.org/10.1016/0167-577X\(95\)00108-5](https://doi.org/10.1016/0167-577X(95)00108-5)
 49. Wang G, Xu DS, Ma N, Zhou N, Payton EJ, Yang R, Mills MJ, Wang Y (2009) Simulation study of effects of initial particle size distribution on dissolution. *Acta Mater* 57:316–325. <https://doi.org/10.1016/j.actamat.2008.09.010>
 50. Ferro P (2013) A dissolution kinetics model and its application to duplex stainless steels. *Acta Mater* 61:3141–3147. <https://doi.org/10.1016/j.actamat.2013.01.034>
 51. Aaron HB, Fainstein D, Kotler GR (1970) Diffusion-limited phase transformations: a comparison and critical evaluation of the mathematical approximations. *J Appl Phys* 41:4404–4410. <https://doi.org/10.1063/1.1658474>
 52. Bian Z, Yang C, Zhu H, Zhao D, Wang M, Zhang H, Chen Z, Wang H (2023) Understanding the creep property of heat-resistant Al alloy by analyzing eutectic phase/matrix interface structures. *Mater Res Lett* 11:205–212. <https://doi.org/10.1080/21663831.2022.2136016>
 53. Robson JD (2020) Deformation enhanced diffusion in aluminium alloys. *Metall Mater Trans A* 51:5401–5413. <https://doi.org/10.1007/s11661-020-05960-5>

Publisher's Note Springer Nature remains neutral with regard to jurisdictional claims in published maps and institutional affiliations.

Springer Nature or its licensor (e.g. a society or other partner) holds exclusive rights to this article under a publishing agreement with the author(s) or other rightsholder(s); author self-archiving of the accepted manuscript version of this article is solely governed by the terms of such publishing agreement and applicable law.

Hongfu Yang is currently working toward the Ph.D. degree in Materials Processing Engineering with the faculty of Material Science and Engineering of Kunming University of Science and Technology, Kunming, China. His research interests include high performance aluminum alloy, advanced steel, and integrated computing materials.

Yelin Zhang is currently working toward the M.S. degree in Materials Engineering with the faculty of Material Science and Engineering of Kunming University of Science and Technology, Kunming, China. Her research interests include high performance aluminum alloy and integrated computing materials.

Shanju Zheng is currently teaching in Faculty of Material Science and Engineering of Kunming University of Science and Technology, Kunming, China. associate professor title. His research interests include high performance aluminum alloy, advanced steel, and integrated computing materials.

Zaki I. Zakib is currently working in the Department of Chemistry, College of Science, Taif University, P.O. Box 11099, Taif 21944, Saudi Arabia.

Rensong Huang is currently working toward the Ph.D. degree in Materials Processing Engineering with the Faculty of Material Science and Engineering of Kunming University of Science and Technology, Kunming, China. His research interests include high performance aluminum alloy and integrated computing materials.

Shumeng Lu is currently working toward the Ph.D. degree in Materials Processing Engineering with the Faculty of Material Science and Engineering of Kunming University of Science and Technology, Kunming, China. His research interests include advanced steel and integrated computing materials.

Peng Sun is currently working toward the Ph.D. degree in Materials Processing Engineering with the Faculty of Material Science and Engineering of Kunming University of Science and Technology, Kunming, China. His research interests include high performance aluminum alloy and integrated computing materials.

Mohamed M. Ibrahim is currently working in the Department of Chemistry, College of Science, Taif University, P.O. Box 11099, Taif 21944, Saudi Arabia.

Mengnie Li is currently working in the Faculty of Material Science and Engineering of Kunming University of Science and Technology, Kunming, China, Professor title. His research interests include integrated computational materials engineering, advanced steel materials, aluminum alloys, copper alloys and titanium alloys and other metal materials.

Xiaohong Yuan is currently working in the Sino-Platinum Metals Co. Ltd., Kunming Institute of Precious Metals, Kunming 650106, China. Her research interests include rare and precious metal materials and microstructure characterization.

Xiaojing Wang is currently working in the Jiangsu University of Science and Technology, Zhenjiang 212003, China. Her research interests include damage and failure of microelectronic interconnect materials and their structures.

Zeinhom M. El-Bahy is currently working in the Department of Chemistry, Faculty of Science, Al-Azhar University, Nasr City 11884, Cairo, Egypt.